



Article

Engineered Mesoporous Silica-Based Core-Shell Nanoarchitectures for Synergistic Chemo-Photodynamic Therapies

Yue-Mei Gao ^{1,†}, Shih-Han Chiu ^{1,†}, Prabhakar Busa ¹ , Chen-Lun Liu ¹, Ranjith Kumar Kankala ^{1,2}
and Chia-Hung Lee ^{1,*}

¹ Department of Life Science, National Dong Hwa University, Hualien 97401, Taiwan

² College of Chemical Engineering, Huaqiao University, Xiamen 361021, China

* Correspondence: chlee016@gms.ndhu.edu.tw; Tel.: +886-3-8903677

† These authors contributed equally to this work.

Abstract: Combinatorial therapies have garnered enormous interest from researchers in efficiently devastating malignant tumors through synergistic effects. To explore the combinatorial approach, multiple therapeutic agents are typically loaded in the delivery vehicles, controlling their release profiles and executing subsequent therapeutic purposes. Herein, we report the fabrication of core (silica)-shell (mesoporous silica nanoparticles, MSNs) architectures to deliver methylene blue (MB) and cupric doxorubicin (Dox) as model drugs for synergistic photodynamic therapy (PDT), chemotherapy, and chemodynamic therapy (CDT). MB, as the photosensitizer, is initially loaded and stabilized in the silica core for efficient singlet oxygen generation under light irradiation towards PDT. The most outside shell with imidazole silane-modified MSNs is immobilized with a chemotherapeutic agent of Dox molecules through the metal (Copper, Cu)-ligand coordination interactions, achieving the pH-sensitive release and triggering the production of intracellular hydrogen peroxide and subsequent Fenton-like reaction-assisted Cu-catalyzed free radicals for CDT. Further, the designed architectures are systematically characterized using various physicochemical characterization techniques and demonstrate the potent anti-cancer efficacy against skin melanoma. Together our results demonstrated that the MSNs-based core-shell nanoarchitectures have great potential as an effective strategy in synergistically ablating cancer through chemo-, chemodynamic, and photodynamic therapies.

Keywords: mesoporous silica nanoparticles; core-shell nanoarchitectures; photodynamic therapy; chemodynamic therapy



Citation: Gao, Y.-M.; Chiu, S.-H.; Busa, P.; Liu, C.-L.; Kankala, R.K.; Lee, C.-H. Engineered Mesoporous Silica-Based Core-Shell Nanoarchitectures for Synergistic Chemo-Photodynamic Therapies. *Int. J. Mol. Sci.* **2022**, *23*, 11604. <https://doi.org/10.3390/ijms231911604>

Academic Editor: János Borbély

Received: 1 September 2022

Accepted: 26 September 2022

Published: 1 October 2022

Publisher's Note: MDPI stays neutral with regard to jurisdictional claims in published maps and institutional affiliations.



Copyright: © 2022 by the authors. Licensee MDPI, Basel, Switzerland. This article is an open access article distributed under the terms and conditions of the Creative Commons Attribution (CC BY) license (<https://creativecommons.org/licenses/by/4.0/>).

1. Introduction

Cancer has emerged as one of the leading reasons of death globally, resulting in millions of deaths annually [1,2]. Over the past decades, several efforts have resulted in understanding the origination, etiology, and development of cancer, resulting in the development of advanced approaches for its early detection and diagnosis [3,4]. Over the past few decades, various therapeutic strategies, such as surgical procedures, radiation, and chemotherapy, have been practiced in ablating cancer [5,6]. In recent times, nanoparticle-based delivery vehicles have become a rapidly growing area in the biomedical field due to their site-specific delivery [7,8], physiological stimulus delivery [9,10], and fewer adverse effects.

Reactive oxygen species (ROS) play an important role in regulating cellular integrity [11,12]. For instance, ROS can be endogenously generated from the NADPH enzyme [13,14] and mitochondrial electron transport chain [15,16]. In cancer therapy, the intracellular generation of excess ROS can provide ablating effects, decreasing cell survival and inhibiting the proliferation of cancer cells [17–19]. Since cancer cells can produce a higher hydrogen peroxide concentration than normal cells, the intracellular provision of metal ions often facilitates ROS production through various catalytic reactions. Typically,

various kinds of toxic ROS, including hydroxyl radicals ($\cdot\text{OH}$), superoxide anions ($\bullet\text{O}_2^-$), and singlet oxygen ($^1\text{O}_2$), can be exogenously produced by photodynamic [20–22], chemodynamic actions, and Fenton-like reactions [23–25]. The imbalance in ROS levels could generate oxidative damages, such as lipid peroxidation, DNA fragmentation, and protein denaturation, triggering cell apoptosis and necrosis [26].

In recent years, the combination of chemo- and photodynamic therapy (PDT), referred to as a synergistic therapeutic strategy, has emerged as the most promising therapeutic strategy in significantly ablating cancer cells. More often, these synergistic therapeutic strategies are operated by administering specific chemo-drugs and photosensitizers that are applicable to localize at the desired site and concomitantly be activated with light to execute their therapeutic effects [27–29]. Despite the advantages and success in killing cancer cells, these photosensitizers for PDT suffer from limitations such as low solubility, poor cellular uptake efficiency, and stability under physiological conditions, subsequently leading to low efficiency. During chemo-photodynamic therapy, several predominant issues must be considered, such as improving their stability and bioavailability in the target cells. Recently, Dong et al. exploited metal- and metal-oxide-based nanoparticles for cancer PDT. Using cerium-based nanoparticles as novel photosensitizers presented an efficient quantum yield for $^1\text{O}_2$ generation and avoided photobleaching effects under light irradiation [30]. In another case, Zhang et al. reported the synthesis of FePS_3 -PEG nanosheets, which showed photothermal effects with good biocompatibility for excellent therapy effects under near-infrared irradiation [31].

Methylene blue (MB), a phenothiazinium photosensitizer, has attracted great interest from researchers in its applications in biomedicine, specifically PDT, due to its high quantum yield of singlet oxygen generation, applicable therapeutic window, and low dark toxicity. However, MB shows the drawbacks to PDT-associated limitations, such as poor stability for photo (or enzyme) degradation and low cell membrane transport. To overcome these limitations, several efforts have been dedicated to developing various inorganic nanoparticles and polymer-based nanocarriers [32,33].

Among various nanocarriers, mesoporous silica-based nanocarriers (MSNs) have gathered massive interest from researchers to deliver various photosensitizers and chemo-drugs due to extensive surface area, high biocompatibility, tunable particle sizes, ease of controlling the functional group distribution, and excellent biocompatibility, among others [34–37]. MSNs have been extensively applied as a carrier in biomedicine and pharmaceutical research, such as imaging [38–40], targeted drug delivery [8,41,42], and gene delivery [43,44], among others [34,35,45]. For instance, Santi et al. synthesized mesoporous silica-loaded MB with amino and mannose-targeted nanoparticles to treat the multi-drug resistance microorganism [46]. Yunhong Yi et al. synthesized plasmonic nanoparticle MB-loaded gold nanobipyramids@ SiO_2 to generate singlet oxygen $^1\text{O}_2$ to treat cancer cells [47].

Inspired by these facts, we fabricated MB- SiO_2 @MSNs core-shell nanocomposites, considering the photosensitizer MB in the silica frameworks as a core, which was coated with imidazole-modified mesoporous silica as a shell to immobilize cupric ion and doxorubicin (Dox) for controlled release through metal coordination for the synergistic effects of chemo-, chemodynamic, and photodynamic therapies (Dox-chemotherapy, cupric ions-CDT, and MB-PDT) to cancer therapeutics (Figure 1). These core-shell architectures were designed to facilitate the embedded MB in the silica frameworks with easy energy transfer to oxygen via mesopores for PDT-based activation to singlet oxygen in ablating cancer cells. Furthermore, the chemotherapeutic drug (Dox) had a high loading rate into the mesopores via metal–ligand affinity interactions from the pH-sensitive copper (Cu)-Dox coordination bond. Dox can additionally induce the production of intracellular hydrogen peroxide in cancer cells; therefore, Cu metal ions in the mesopores synergistically enhance the ROS levels by catalytic cycles through the Fenton-like reactions.

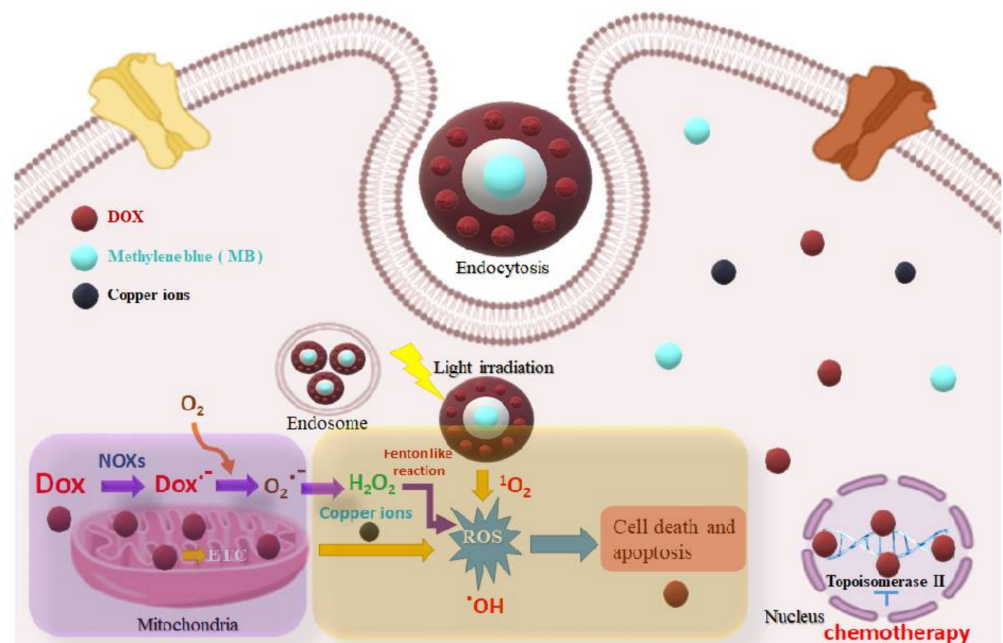


Figure 1. Schematic representing the plausible mechanisms of the core-shell nanocomposites for chemo-, chemodynamic, and photodynamic therapies.

2. Results and Discussion

As shown in the schematic illustration (Figure 2), this work accomplishes all the following aspects. Initially, we prepared MB-SiO₂ nanoparticles, in which the photosensitizer MB molecules were monodispersed in the silica framework to avoid aggregation. In addition, the negative charges of the silica skeleton form strong electrostatic interactions with MB to further improve the stability of the photosensitizer and the energy transfer efficiency of PDT. Further, the growth of mesoporous silica shells on the MB-SiO₂ can increase the stability of MB molecules to prevent their leaching during the delivery processes. The MB-SiO₂@MSNs showed fine spherical morphological structures of core-shell nanoparticles. After removal of CTAB⁺ by isopropanol-based chemical extraction, mesopores were modified with imidazole silane for Cu ion chelation. The use of metal affinity interactions can achieve the high loading of Dox along with pH-sensitive controllable release to enhance their efficiency for chemo-photodynamic combination therapy towards melanoma cancer cells.

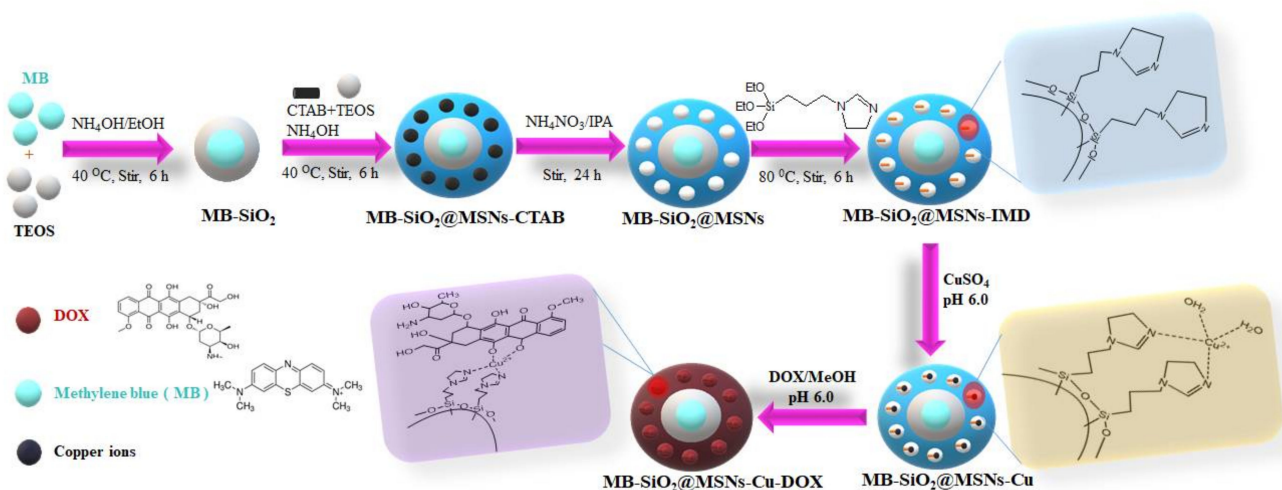


Figure 2. Schematic representation showing the synthesis of MB core-shell nanoparticles with surface modification of imidazole group for metal coordination and further immobilization of Dox.

2.1. Preparation and Characterization of MB-SiO₂@MSNs

The TEM image of MB-SiO₂ nanoparticles (Figure 3A) revealed that the MB-SiO₂ NPs showed a spherical shape with an average diameter of 50 nm. The spherical MB-SiO₂ with a highly dense core facilitated the successful encapsulation of MB in the silica frameworks with tunable morphology and size. Further, mesoporous silica was grown on the surface of MB-SiO₂ by the sol-gel co-condensation method. The results showed that MSN shells with the proper thickness (20 nm) and porous structures existed in the outside shells of the nanocomposites. Together, the overall morphology of the designed MB-SiO₂@MSNs core-shell nanoarchitectures was a spherical and uniform diameter of around 200 nm, with a uniform mesoporous shell (Figure 3B–D).

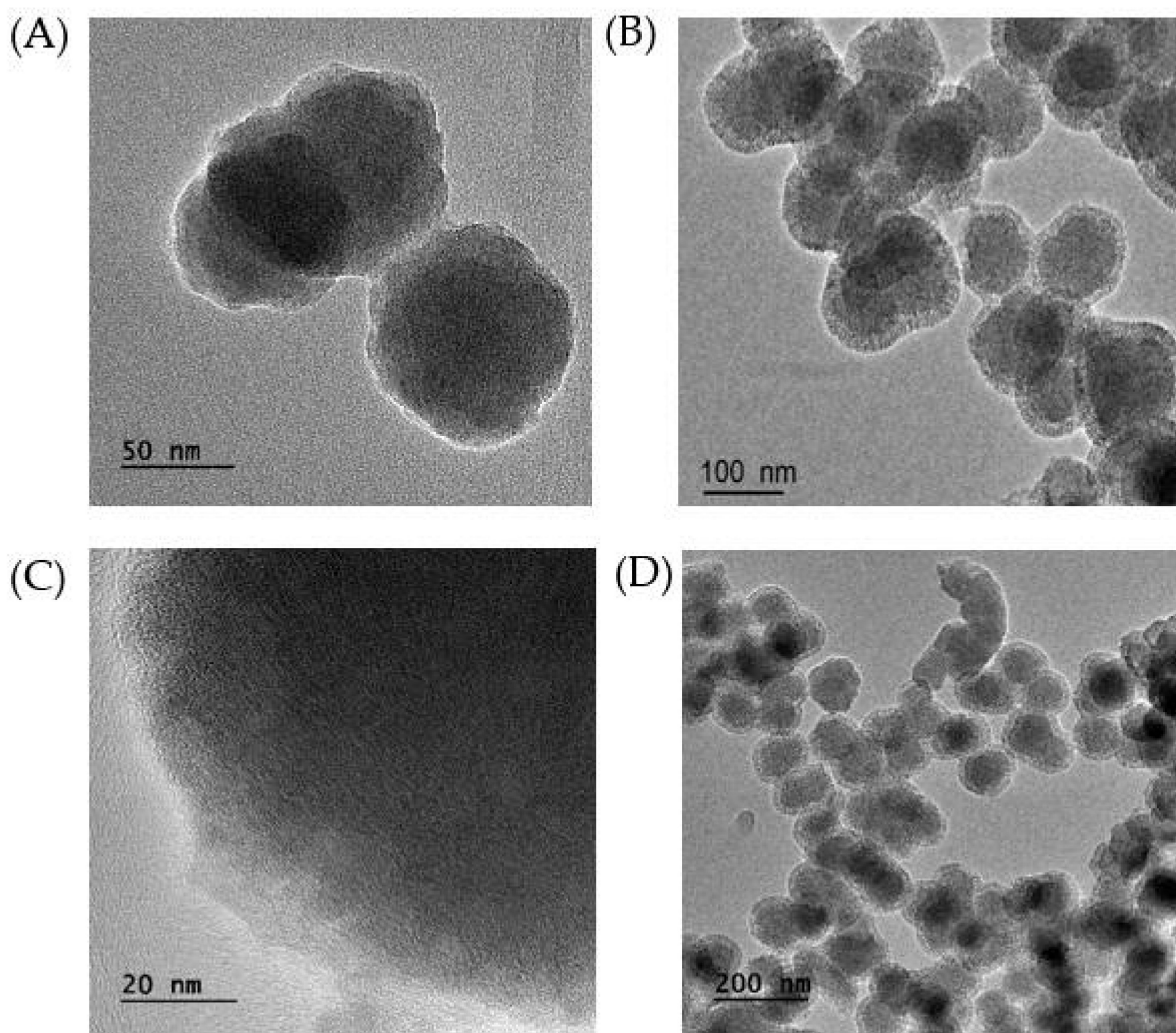


Figure 3. TEM images of (A) MB-SiO₂ and (B–D) MB-SiO₂@MSNs nanocomposites.

Further, the textural properties of surface area, pore volume, and pore size of as-synthesized MB-SiO₂@MSNs, surfactant extracted MSNs, silane modification, cupric coordination, and Dox loading were determined by nitrogen adsorption–desorption isotherms using the Brunauer–Emmett–Teller method (BET). As depicted in Figure 4A, the adsorption–desorption curve represents a type-IV isotherm with a small hysteresis loop. Due to the prominent condensation step at high relative pressure, the dried nanoparticles showed heavily agglomerated forms and nitrogen condensation in the interparticle voids. The adsorption isotherm of as-synthesized MB-SiO₂@MSNs showed less surface area (256 m²/g) and pore volume (0.650 cm³/g), indicating that the nanochannels were blocked by CTA⁺

surfactants (Table 1). After extraction of CTA⁺ by NH₄NO₃/isopropanol solution, the surface area and pore volume drastically increased to 818 m²/g and 1.044 cm³/g, respectively. These results suggested the successful synthesis of MB-SiO₂@MSNs with mesoporous structures and huge surface area. Furthermore, the surface-modified, cupric-coordination, and Dox-loaded samples showed a gradual decrease in their surface areas and pore volumes (MB-SiO₂@MSNs-IMD: 386 m²/g, 0.592 cm³/g; MB-SiO₂@MSNs-Cu: 380 m²/g, 0.486 cm³/g; and MB-SiO₂@MSNs-Cu-Dox: 249 m²/g, 0.439 cm³/g) [48,49]. Considering these textural properties, it should be noted that the Cu-Dox complexes were well dispersed and immobilized inside the nanochannels of MSNs by imidazole silane. Specifically, the pore size analysis showed that the imidazole silane-modified MB-SiO₂@MSNs samples were reduced from 2.5 to 2.1 nm. Subsequently, the loadings of Cu and Dox resulted in the further reduction of pore sizes of the designed nanoarchitectures (Figure 4B). It should be noted that the BJH method would underestimate the pore size distribution of the mesoporous samples [50]. However, in comparison between the samples, it could be concluded that the reduction in the surface area, pore volume, and pore diameter indicated the successful modification of MB-SiO₂@MSNs and immobilization of Cu and Dox in the nanochannels of MSNs.

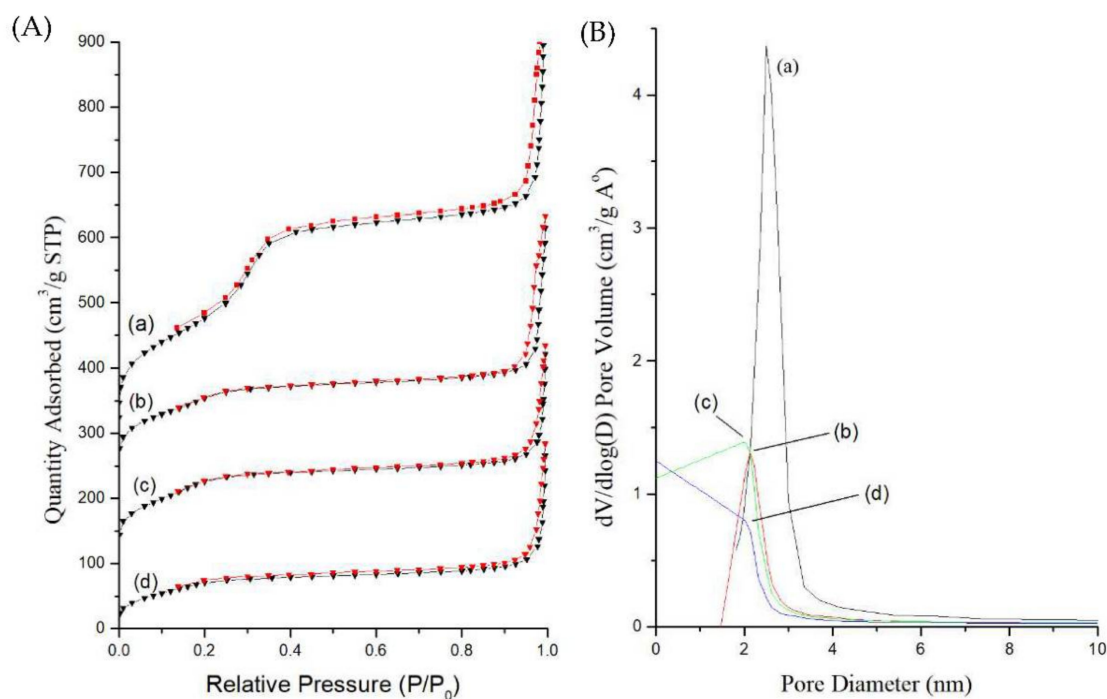


Figure 4. (A) Nitrogen adsorption (black line)–desorption (red line) isotherms and (B) pore size distribution plots of (a) MB-SiO₂@MSNs (black line), (b) MB-SiO₂@MSNs-IMD (red line), (c) MB-SiO₂@MSNs-Cu (green line), and (d) MB-SiO₂@MSNs-Cu-Dox (blue line).

Table 1. Textural properties of the various nanocomposites.

Sample	Surface Area ^a (m ² g ^{−1})	Pore Volume ^b (cm ³ g ^{−1})	Pore Diameter ^c (nm)
MB-SiO ₂ @MSNs-CTA ⁺	256	0.650	N.D. ^d
MB-SiO ₂ @MSNs	818	1.044	2.5
MB-SiO ₂ @MSNs-IMD	386	0.592	2.1
MB-SiO ₂ @MSNs-Cu	380	0.486	N.D. ^d
MB-SiO ₂ @MSNs-Cu-Dox	249	0.439	N.D. ^d

^a Determined by the BET method. ^b Determined by the t-plot method. ^c Determined by the BJH method in the adsorption branch of the isotherm. ^d N.D. = Not determined.

Further, the successive immobilization of organic groups, including drugs, was confirmed by the thermogravimetric analysis (TGA) and derivative thermogravimetry (DTG) of MB-SiO₂, MB-SiO₂@MSNs-IMD, and MB-SiO₂@MSNs-Cu-Dox. Figure 5A refers to the total weight loss curves, and Figure 5B denotes the derivation weight loss curves. The initial decomposition of all the samples in the heating process below 100 °C could be due to the loss of adsorbed water on the nanoparticle surfaces. Further, the weight loss after 100 °C could be due to the combustion of organic composites of imidazole silane, MB, and Cu-Dox in the MB-SiO₂@MSNs-Cu-Dox. For the MB-SiO₂@MSNs-IMD sample, the decomposition temperature of over 250 °C could be attributed to the weight loss due to imidazole groups. The MB-SiO₂@MSNs-Cu-Dox in TGA studies showed an additional peak at 417 °C, which could be accumulated weight loss of organic modification and Dox degradation. The delayed degradation might have occurred due to chelation formation with quinolone moieties with Cu ions, respectively. The final loading amount of Dox was calculated as 7.5%, compared with bare MSNs (i.e., 2% wt of MSNs). Together, these findings indicated that the increased loading percentage of Dox was due to metal–ligand interactions with Cu (II) and Dox compared to Dox loaded in bare MSNs, which happened due to physical adsorption.

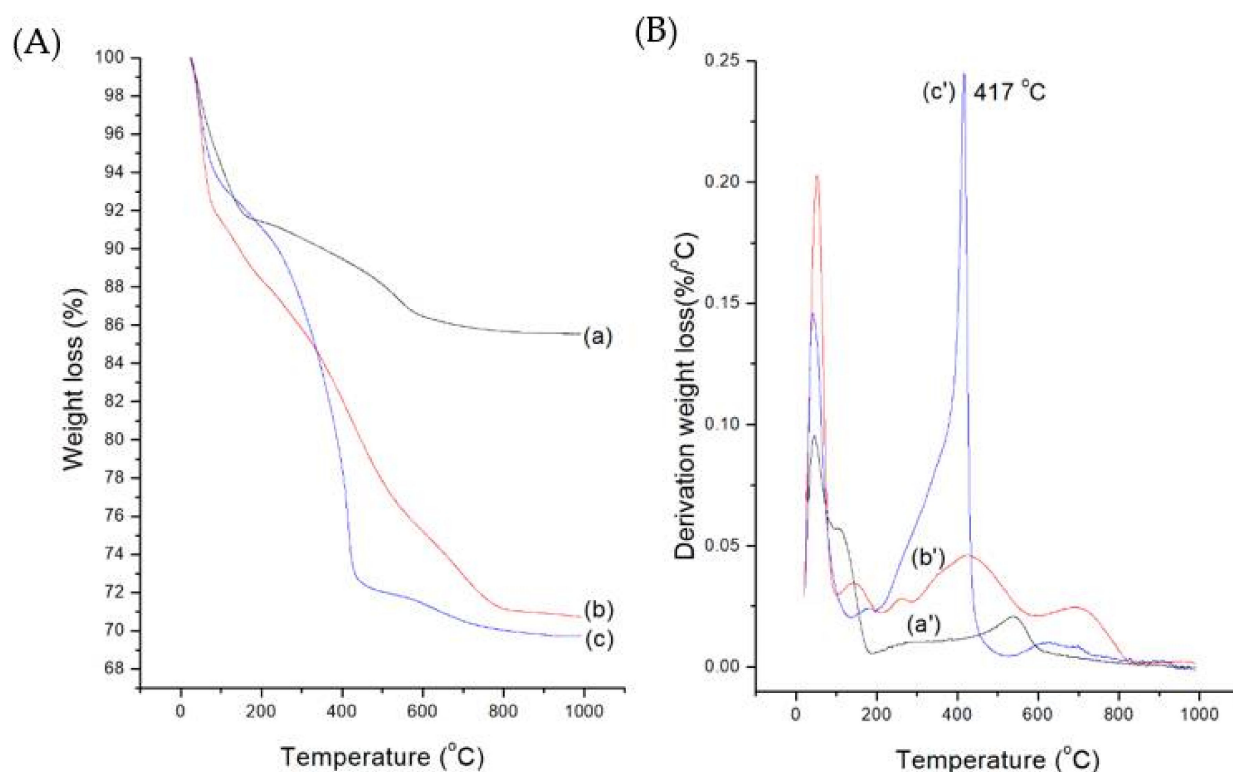


Figure 5. (A) TGA of weight loss profiles and (B) DTG profiles from the derivative weight loss of (a) MB-SiO₂, (b) MB-SiO₂@MSNs-IMD, and (c) MB-SiO₂@MSNs-Cu-Dox.

Further, FT-IR spectroscopy was employed to explore the successful immobilization of chemical functionalities of the silica backbone and the organic groups in the designed core-shell nanocomposites (Figure 6). The broad spectrum at 3423 cm⁻¹ could be ascribed to the O-H stretch of surface Si-OH and adsorbed water molecules (Figure 6a). The characteristic peaks at 1083 cm⁻¹ and 792 cm⁻¹ could be attributed to the Si-O-Si frameworks, resulting in the formation of stable silica structures. The high-intensity peaks at around 2851 to 2920 cm⁻¹ and the C-H deformation peak at 1500 cm⁻¹ could correspond to C-H stretching, indicating the CTA⁺ surfactant template of the MB-SiO₂@MSNs-CTA⁺ sample (Figure 6b). After the surfactant was extracted in ammonium nitrate/isopropanol solution, the C-

H stretching characteristic peaks were significantly reduced, indicating the successful extraction of the surfactant and resulting in the mesopores.

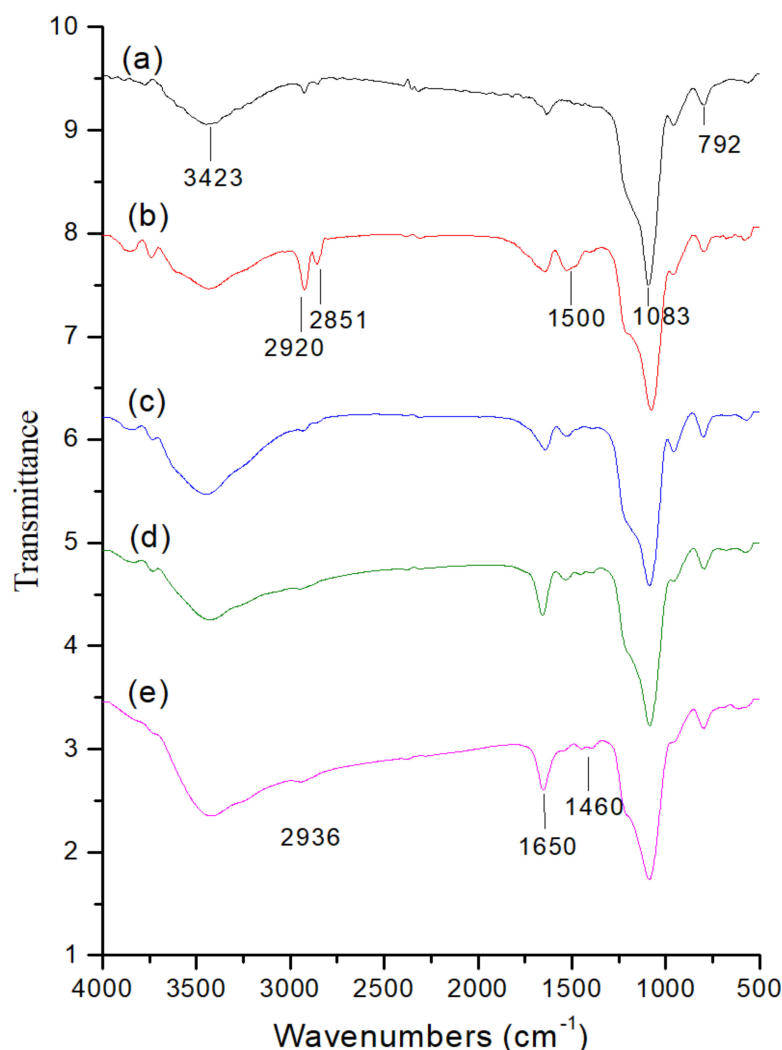


Figure 6. FT-IR spectra of (a) MB-SiO₂, (b) MB-SiO₂@MSNs-CTA⁺, (c) MB-SiO₂@MSNs, (d) MB-SiO₂@MSNs-IMD, and (e) MB-SiO₂@MSNs-Cu-Dox.

In the case of the Dox-loaded core-shell sample, the peak intensity at 1460, 1650, and 2936 cm⁻¹ increased, which could be due to N-H, carbonyl, and C-H vibrational stretches of Dox, confirming its successful encapsulation in MB-SiO₂@MSNs-Cu sample (Figure 6e) [51].

Next, the ESR spectroscopy was applied to explain the characteristic feature of the Cu (II) coordination in the nanocomposites with 3d⁹ electronic spin ($S = 1/2$) and nuclear spin ($I = 3/2$). The spectrum of Figure 7A showed an anisotropic Cu(II) signal at 77 K. The calculated g values revealed that Cu(II) formation started sharing electrons in the nitrogen atoms of the imidazole ring and Dox quinone oxygen moieties. The g values, i.e., g_{\parallel} (2.26) > g_{\perp} (2.06), resulted due to the lone paired electrons' characteristic spin in tetragonally elongated coordination (Figure 7A(a)). After a release study of the MB-SiO₂@MSNs-Cu-Dox sample in phosphate-buffered saline (PBS, pH 5.0), we observed that the g value was near 2.0, due to the disassociation of pH-sensitive coordination bond expelling the Cu-Dox from the NPs (Figure 7A(b)). The PBS (pH 5.0)-soaked NPs had decreased Cu(II) signal, evidencing that Dox had a successfully triggered release by metal-ligand coordination [9].

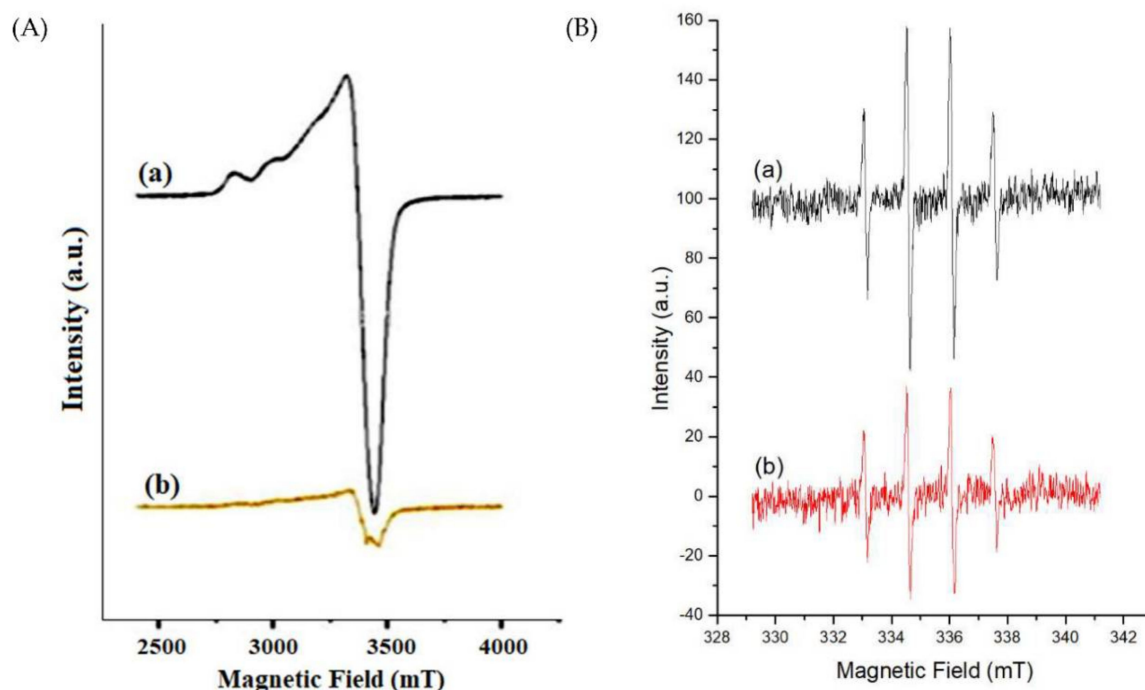
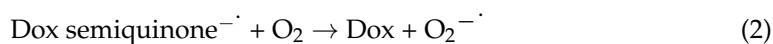
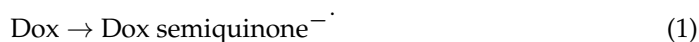
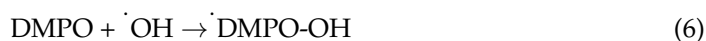
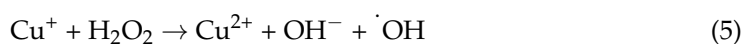


Figure 7. ESR spectra of (A) MB-SiO₂@MSNs-Cu-Dox sample (a) before and (b) after release study in phosphate buffer (pH 5.0); (B) Spin trapping signal of \cdot DMPO-OH radical arising from (a) MB-SiO₂@MSNs-Cu, and (b) MB-SiO₂@MSNs-Cu-Dox sample reacted with H₂O₂.

Since Dox can trigger intracellular production of H₂O₂ levels, the mechanism for H₂O₂ production in CDT using the MB-SiO₂@MSNs-Cu-Dox sample is represented in Equations (1)–(3). Dox is initially activated to a semiquinone radical in the mitochondrion (Equation (1)). Further, the oxygen species in the presence of semiquinone radicals reduce to superoxide by one-electron transfer (Equation (2)). Finally, the superoxide dismutation results in the generation of H₂O₂ (Equation (3)). In this study, the MB-SiO₂@MSNs-Cu-Dox nanoparticles are internalized by cancer cells, triggering the pH-sensitive release of Dox in the acidic pH of endosomes. Thus, the released Dox can increase the intracellular H₂O₂ levels and catalyze the Cu(II) ions to produce cytotoxic hydroxyl radicals.



To further prove that Cu(II) ions in MB-SiO₂@MSNs samples could catalyze a Fenton-like reaction (Equations (4) and (5)) to generate free radicals for CDT, we used a spin trapping technique to capture the active free radicals during the reaction (Equation (6)). The resultant hydroxyl radicals could be trapped by DMPO to form a \cdot DMPO-OH adduct as a stable radical. After the reaction, the liquid phase of extracted solution showed a signal of 1:2:2:1 hyperfine splitting pattern ($a_N = a_{H\beta} = 1.496$ mT). The signal intensities of \cdot DMPO-OH in MB-SiO₂@MSNs-Cu and MB-SiO₂@MSNs-Cu-Dox samples are displayed in Figure 7B. The EPR intensity showed that the MB-SiO₂@MSNs-Cu sample displayed a high concentration of active Cu(II) ions in the Fenton-like reaction.



2.2. Cellular Uptake Studies

Typically, the nanoparticles enter cells through endocytosis pathways, the gateway into the cell [52,53]. It was observed that the designed FITC-conjugated MB-SiO₂-MSNs showed high stability and cell uptake efficiency without leaching of MB. The NPs were internalized by the endocytosis mechanism, and a large number of nanoparticles were localized in the cytoplasm (Figure 8A). MB-SiO₂@MSNs without Dox were non-toxic at high levels of nanoparticle concentration. Furthermore, achieving high Dox loading through Cu(II) metal affinity could trigger Dox release under the acidic pH of endosomes. The fluorescent images of DAPI staining after being treated with MB-SiO₂@MSNs-Cu-Dox in B16 cancer cells successfully induced cell apoptosis, resulting in the change of nuclear morphology and chromatin condensation (Figure 8B).

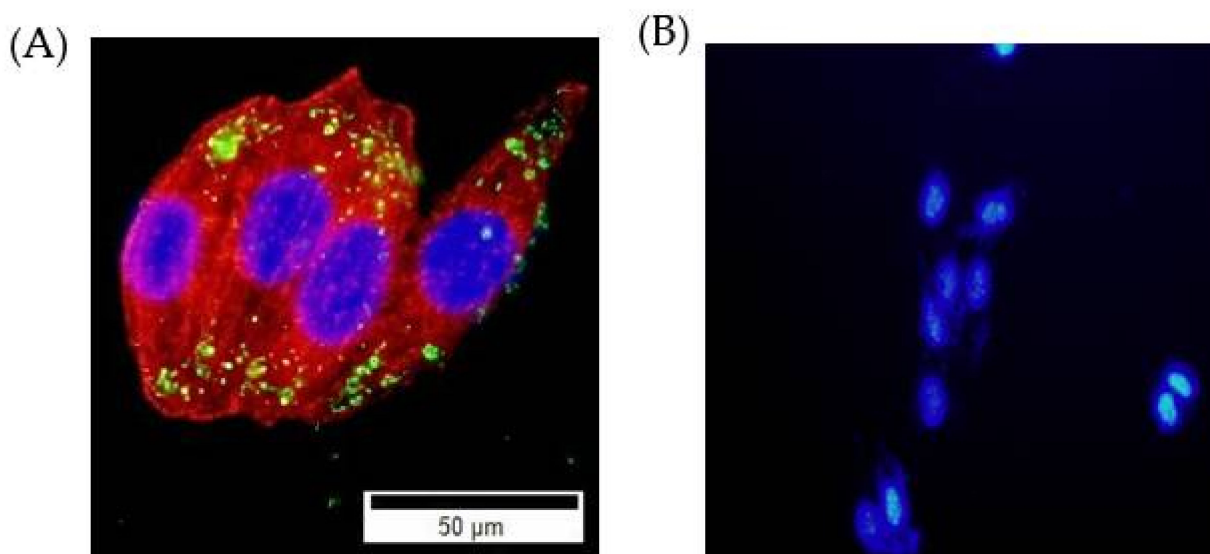


Figure 8. Fluorescent images to evaluate cell uptake of (A) FITC-labeled SiO₂@MSN nanocomposites (green); cytoskeleton of rhodamine-phalloidin staining (red); DAPI nuclear staining (blue), and (B) MB-SiO₂@MSNs-Cu-Dox-treated cells (with light) produced apoptotic bodies of condensed chromatin with bright fluorescence.

2.3. ROS Studies

Further, we used a 2',7'-dichlorofluorescein diacetate (DCFH-DA) probe to measure the intracellular reactive oxygen species (ROS) production. Typically, DCFH-DA enters the cells by passive diffusion, resulting in the cleavage of the two acetate groups of DCFH-DA and conversion into non-fluorescent DCFH by intracellular esterases. The oxidation of DCFH by various ROS (or H₂O₂) can generate highly fluorescent DCF, which shows excitation and emission at 485 nm and 535 nm. The treatments of MB-SiO₂@MSNs and MB-SiO₂@MSNs-Cu-Dox samples in the presence or absence of light irradiation were measured for ROS production by flow cytometric assay (Figure 9). Compared with the control group (no drug/nanoparticle treatments) and MB-SiO₂@MSNs (dark) sample, the MB-SiO₂@MSNs (light) sample showed a slight increase in ROS, mainly attributable to the photodynamic effects of MB. In addition, the MB-SiO₂@MSNs-Cu-Dox (dark) treated cells showed a further increase in ROS levels. The maximum ROS production was observed under the light irradiation of the MB-SiO₂@MSNs-Cu-Dox sample, indicating a combination of the synergistic effects from PDT effects of MB, chemotherapy of Dox, and chemodynamic therapy of copper ions. The ratios of mean fluorescence are 1: 1.2: 3.2: 2.6: 5.5 for the control, MB-SiO₂@MSNs (dark), MB-SiO₂@MSNs (light), MB-SiO₂@MSNs-Cu-Dox (dark), and MB-SiO₂@MSNs-Cu-Dox (light) sample. Thus, the ratios of ROS production contributed to from PDT only: chemotherapy, and CDT: PDT, chemotherapy, and CDT are 1.43:1:3.07.

The results demonstrated that the combination of three synergistic effects could effectively produce the maximum levels of ROS and further induce DNA damage and cell death.

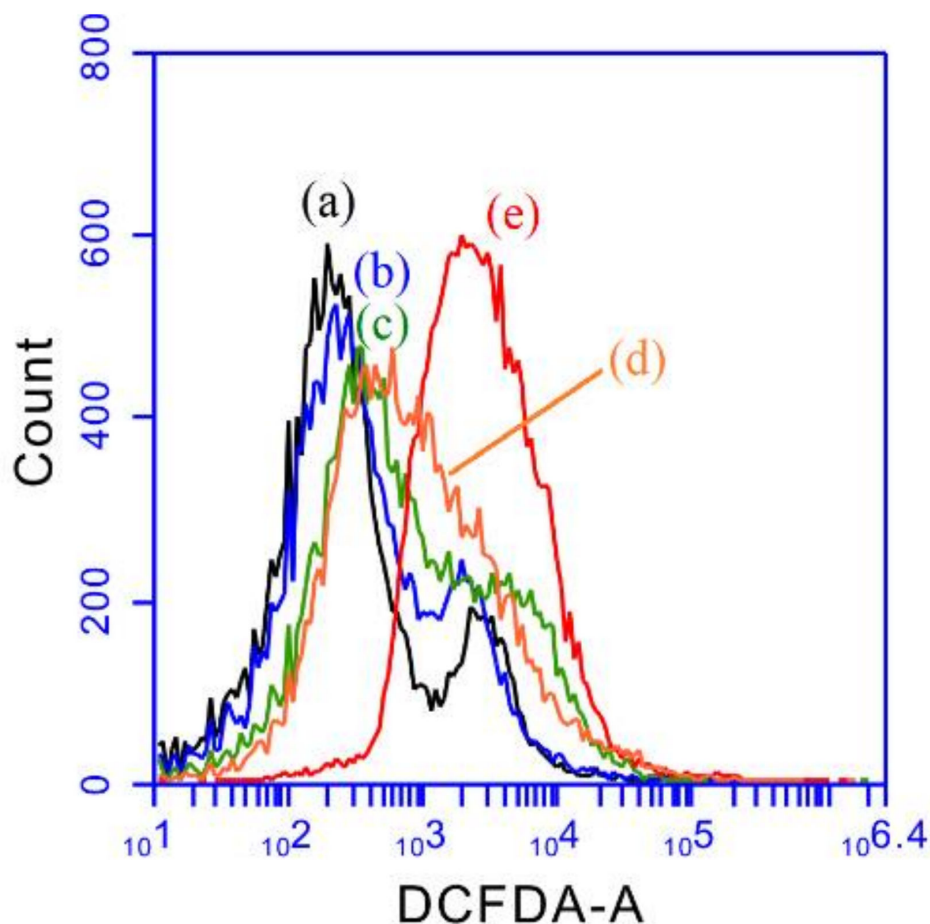


Figure 9. Evaluation of intracellular ROS by using DCFH-DA assay of (a) control (no nanoparticle treatment), (b) MB-SiO₂@MSNs (dark), (c) MB-SiO₂@MSNs (light), (d) MB-SiO₂@MSNs-Cu-Dox (dark), and (e) MB-SiO₂@MSNs-Cu-Dox (light) at the concentration of 50 µg/mL.

2.4. DNA Damage Studies

Further, we used a comet assay of single cell gel electrophoresis to measure DNA damage from double (or single) strand breaks by nanoparticles. Our results showed that the MB-SiO₂@MSNs-IMD-Cu sample induced a slight break for DNA with fewer signals for the comet tail (Figure 10). However, the MB-SiO₂@MSNs-Cu-Dox-treated cells damaged most DNA, resulting in long-tailed comet signals. The mechanism lies in that the released Dox molecules could generate high levels of H₂O₂ concentration in cancer cells. Furthermore, Cu(II) ions could catalyze the H₂O₂ to produce highly toxic hydroxyl radicals and attack DNA for CDT. The MB-SiO₂@MSNs-Cu-Dox sample was irradiated with light, generating the MB-assisted PDT efficacy and resulting in a large amount of singlet oxygen. Thus, the synergistic effect of PDT and CDT could trigger the heavy damage of DNA to break into smaller fragments.

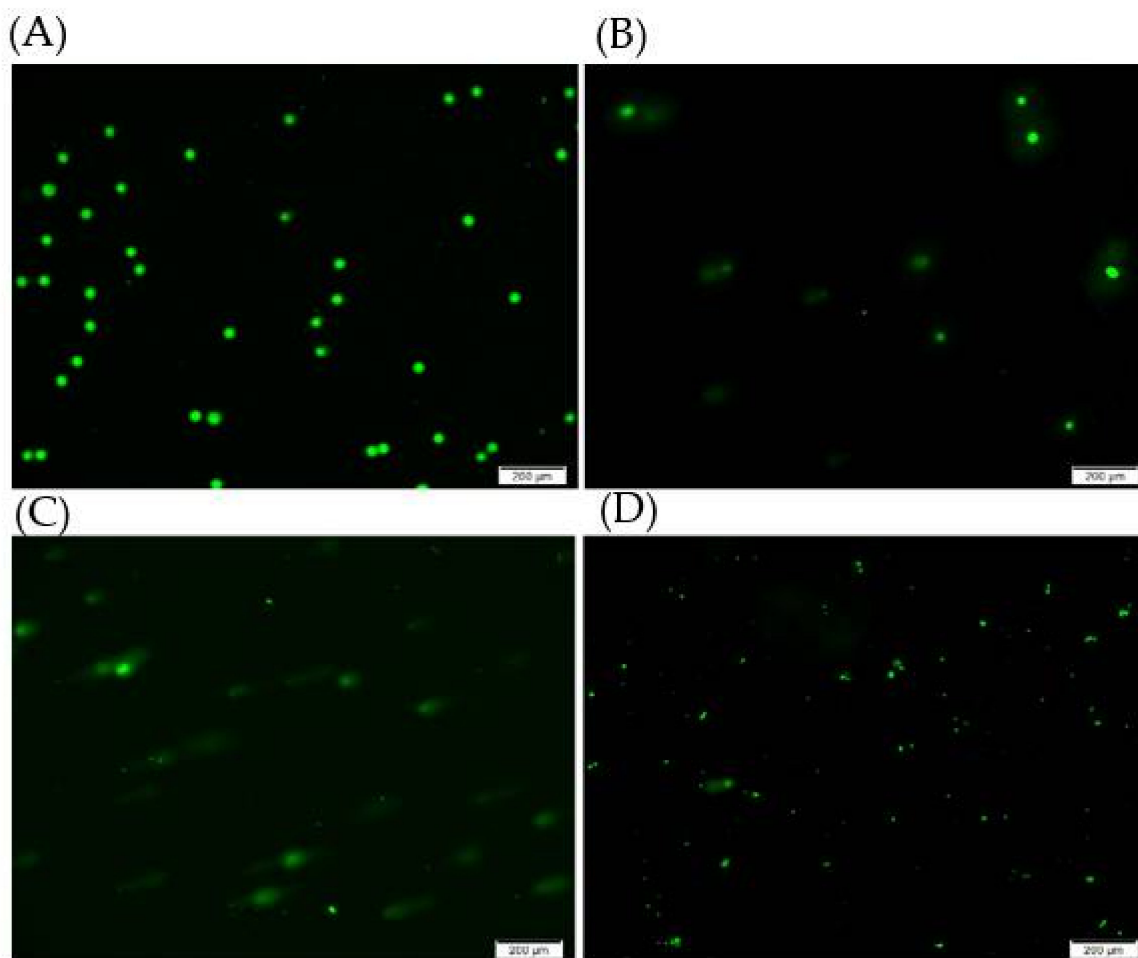


Figure 10. Comet assay from the single cell gel electrophoresis of B16 melanoma cells with (A) control (no nanoparticle treatment), (B) MB-SiO₂@MSNs-IMD-Cu, (C) MB-SiO₂@MSNs-Cu-Dox, and (D) MB-SiO₂@MSNs-Cu-Dox (with light) at the concentration of 50 μg/mL.

2.5. Cytotoxicity Studies

Indeed, the potential toxicity of the carrier is always a great concern for nanomaterials used in drug delivery. To explore these aspects, we examined whether the delivery system would induce significant cytotoxicity in cancer cells under dark or light conditions (LED 630 nm, 15 mW/cm² for 15 min). The cytotoxicity and anti-cancer activity of the designed nanocomposites were explored by incubation of various concentrations of nanoparticles for 24 h. As shown in Figure 11A, MB@SiO₂ and MB-SiO₂@MSNs samples without light irradiation showed low cytotoxicity. However, the MB-SiO₂@MSNs-Cu-Dox-treated cells demonstrate a dose-dependent cytotoxic effect against B16 cells (Figure 11B). Further, the synergistic effect of nanocomposite with and without light irradiation was evaluated. The cell viability of MB-SiO₂@MSNs (dark), MB-SiO₂@MSNs (light), MB-SiO₂@MSNs-Cu-Dox (dark), and MB-SiO₂@MSNs-Cu-Dox (light) at 6.26 μg/mL treatment was 96%, 80%, 59%, and 47%, respectively. Therefore, the therapeutic effects from PDT only, chemotherapy plus CDT, and PDT plus chemotherapy plus CDT were in the ratios of 1:2.31:3.06. The combination therapy was proceeded by irradiation and further incubation for 20 h with MB-SiO₂@MSNs-Cu-Dox nanocomposites. In the presence of a light source, MB absorbed the light kinetic energy and produced PDT to inhibit cell growth. Dox can perform chemotherapy and inhibit the progress of cell division. Moreover, the intracellular liberated Cu ions were involved in the Fenton-like reaction and produced free radicals to enhance the anti-cancer activity of CDT [54–58].

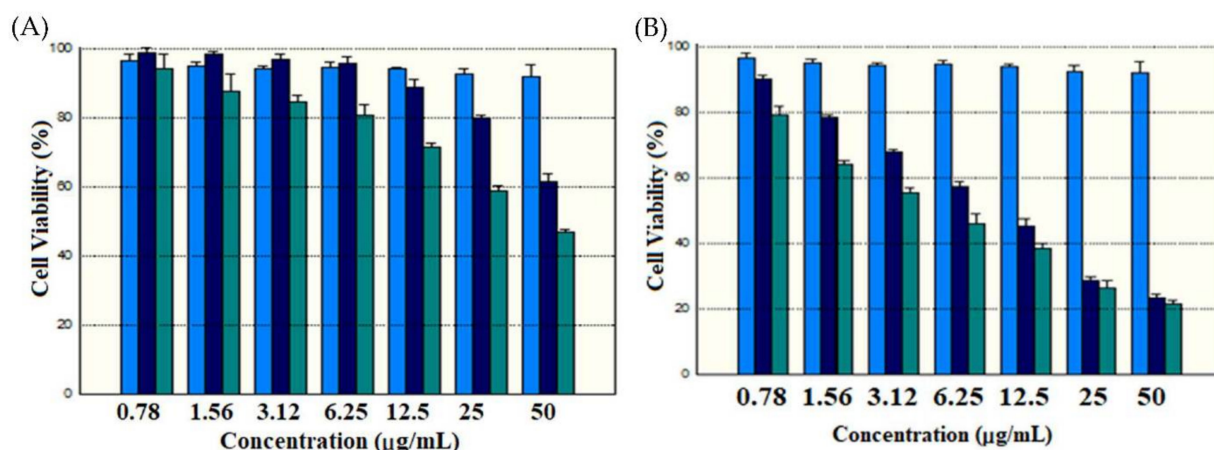


Figure 11. Cell viability by SRB assay of B16 melanoma cells after treatment of (A) MB-SiO₂ (light blue), MB-SiO₂@MSNs without light (dark blue), and MB-SiO₂@MSNs with light (green) and (B) MB-SiO₂ (light blue), MB-SiO₂@MSNs-Cu-Dox without light (dark blue), and MB-SiO₂@MSNs-Cu-Dox with light (green) at various nanoparticle concentrations.

3. Materials and Methods

3.1. Materials

Cetyltrimethylammonium bromide (CTAB), fluorescein isothiocyanate (FITC), and tetraethoxysilane (TEOS) were obtained from Acros Organics Ltd. (Geel, Belgium). Potassium bromide was acquired from Fisher Scientific Ltd. (Loughborough, UK). Sulforhodamine B (SRB), ammonium nitrate (NH₄NO₃), N-(3-triethoxysilylpropyl)-4,5-dihydroimidazole, MB, and 2',7'-dichlorofluorescein diacetate (DCFH-DA) were purchased from Sigma. Co. Ltd. (St. Louis, MO, USA). Copper sulfate was obtained from Showa Chemical Co. Ltd. (Gyoda, Japan). DMEM medium and Fetal bovine serum (FBS) were acquired from GIBCO/BRL Life Technologies (Grand Island, NE, USA). The comet assay kit was obtained from R&D systems (Minneapolis, MN, USA). Diamidino-2-phenylindole dihydrochloride (DAPI) and rhodamine-phalloidin were purchased from Invitrogen Ltd. (Eugene, OR, USA).

3.2. Characterizations

The micrometric surface area analyzer ASAP 2020 (Norcross, GA, USA) was used to determine N₂-adsorption and desorption isotherms at 77 K for analyzing the textural properties. The surface area of various samples was obtained by the BET method. The pore size distribution curves were analyzed for the adsorption portion of the isotherms using the BJH (Barrett–Joyner–Halenda) method. The pore volume was obtained from the t-plot method. The chemical functional groups were confirmed by recording Fourier transform infrared (FT-IR) spectra on an Alpha spectrometer (Bruker, Billerica, MA, USA). Electron spin resonance (ESR) spectra were recorded using an EMX spectrometer (Bruker, Billerica, MA, USA) measured at 77 K. The physical composition of the nanoparticles was determined using thermogravimetric analysis (TGA) from the TA instruments. The surface morphology was determined by the transmission electron microscopy (TEM) images captured on a Hitachi H-7100 (Tokyo, Japan) operated at 100 kV.

3.3. Synthesis of MB@SiO₂ Nanoparticles

Briefly, MB-incorporated non-porous silica nanoparticles as cores were synthesized using the previous procedure with slight modifications [59,60]. Initially, 14.5 mL of TEOS and 0.4 mL of MB (10 mg/mL of stock solution in deionized water) were added into a beaker containing 65.7 mL of ethanol (95%) and stirred for 20 min at 40 °C. Further, 4.9 mL of ammonia solution (28%) was added to the mixture and then stirred for another 6 h at the same temperature [61]. The MB-entrapped silica nanoparticles were collected by

centrifugation and washed with ethanol. The nanoparticles were further dispersed in ethanol solution and stored at 4 °C. The product was named MB-SiO₂.

3.4. Synthesis of MB-SiO₂@MSNs

The mesoporous silica shell over the MB-SiO₂ cores was grown using the conventional Stöber co-condensation method. Briefly, CTAB (300 mg) was completely dissolved in dd-H₂O (60 mL). Then, 100 mg of MB@SiO₂ was added to the above solution along with 1.1 mL of ammonia solution (28%), and the total mixture was stirred at a constant speed for 30 min at 40 °C. Further, the silica source, TEOS (0.5 mL), was added and stirring continued for another 6 h. The resultant core-shell solids were collected by centrifugation and washed twice with ethanol. Considering the templating mechanism, the CTAB molecules could be encapsulated as templates in cetyltrimethylammonium ion (CTA⁺). The product was shortly denoted as MB-SiO₂@MSNs-CTA⁺. Finally, the template was removed via a highly efficient chemical extraction approach. The as-synthesized MB-SiO₂@MSNs-CTA⁺ were dispersed in isopropanol (IPA, 50 mL) containing ammonium nitrate (NH₄NO₃, 30 mg) and continuously stirred for 24 h at 85 °C. Finally, the resultant product was collected by centrifugation (12,000 rpm for 17 min) and washed twice each with water and ethanol. The product was named as MB-SiO₂@MSNs [62]. FITC-labeled MB-SiO₂@MSNs were synthesized through the reaction of 3-aminopropyltriethoxysilane (APTES) with FITC molecules. Briefly, FITC (1 mg) and APTES 10 µL were dissolved in dried methanol (1 mL) and stirred at room temperature for 18 h in the dark. Further, FITC-labeled MB-SiO₂@MSNs were synthesized by the same procedure of MB-SiO₂@MSNs synthesis, except that the APTES-FITC conjugation was added to the TEOS beforehand. The co-condensation reaction proceeded in the dark.

3.5. Synthesis of Imidazole-Modified MB-SiO₂@MSNs

Initially, 100 mg of MB-SiO₂@MSNs was added to 80 mL of toluene and allowed to stir for 20 min. Then, 0.5 mL of N-(3-triethoxysilylpropyl)-4, 5-dihydroimidazole silane was added, and stirring continued for 6 h at 80 °C. The imidazole silane-modified nanoparticles were collected by centrifugation (12,000 rpm for 17 min) and washed with water and ethanol twice each. Finally, the product was denoted shortly as MB-SiO₂@MSNs-IMD [63,64].

3.6. Coordination of Cupric Ions onto MB-SiO₂@MSNs-IMD Nanoparticles

More often, the transition metals coordination is favorable by Lewis acid and base interactions between nitrogen and Cu atoms. Initially, 180 mg of copper sulfate as a Cu source was dissolved in 30 mL of dd-H₂O at pH-6.0. Then, 200 mg of previously prepared MB-SiO₂@MSNs-IMD was added and stirred for 30 min. The collected product by centrifugation (12,000 rpm for 17 min) was washed twice with ethanol and denoted as MB-SiO₂@MSNs-Cu [65,66].

3.7. Immobilization of Dox onto MB-SiO₂@MSNs-Cu

The anthraquinone functional group of Dox contains a lone pair of electrons, which could participate in a chelation reaction, resulting in the acidic pH-responsive coordination bond with metal ions. First, 5 mL of methanolic Dox solution at a concentration of 1.0 mg/mL was added with 100 mg of MB-SiO₂@MSNs-Cu nanoparticles, and the pH of the mixture was adjusted to 6.0 and stirred for 24 h. The resultant solid was collected by centrifugation (12,000 rpm for 17 min) and washed twice with ethanol. The product was denoted as MB-SiO₂@MSNs-Cu-Dox [67,68].

3.8. Cell Culture

The mouse melanoma cells (B16 cell line) were cultured in a DMEM medium with 10% FBS and 1% antibiotics (penicillin/streptomycin) maintained at 37 °C in 5% CO₂.

3.9. SRB Assay

Initially, cells (1×10^5 cells per well) were seeded in a 96-well plate and incubated overnight. Further, one control was fixed with trichloroacetic acid (TCA, 25 μ L of 50% *w/v*) to arrest the cell cycle. Furthermore, the treatment groups and another control group were continued for further experiments. The treatment groups were added with different concentrations of nanoparticle samples dispersed in 100 μ L of the medium. After 4 h of incubation, the respective treatment groups were subjected to the light treatment by using a LED 630 nm (15 mW/cm²) for 15 min and further incubation for 20 h. Later, 50 μ L of cold TCA (50%) was added to other wells and incubated at 4 °C for 1 h. After decanting the medium and water washes, 100 μ L of 0.4% (*w/v*) SRB solution (in 1% acetic acid) was added to all the wells and incubated for 20 min. The excess SRB was removed and further washed by using 1% (*v/v*) of acetic acid and subsequently solubilized by adding 10 mM of Trizma base (pH 10.5). Finally, the absorbance values were measured at 515 nm. Finally, the cell viability was calculated from the formula of $[(\text{Ctl} - \text{T}_x)/(\text{Ctl})] \times 100$ [69].

3.10. Cellular Uptake Studies

Initially, cells at a density of 5×10^5 cells were seeded in a 10 cm culture dish and incubated for 24 h for cell attachment. Then, 1 mL of FITC-conjugated nanoparticles (50 μ g/mL) were dispersed in a medium and incubated for 24 h. Further, the culture medium was removed and washed twice with PBS. Then, a series of steps were followed to prepare the cells for immunostaining of fluorescent imaging, formalin (3.7%, 1 mL, 10 min) for cell fixation, Triton X-100 (0.1% in PBS, 1 mL, 5 min) for cell membrane permeation, BSA (3%), rhodamine-phalloidin (1 μ g/mL, 30 min) for staining cytoskeleton, and DAPI (2 μ g/mL, 5 min) for counterstaining nucleus. Finally, the cells were visualized under fluorescence microscopy [70,71].

3.11. Comet Assay

Single-cell gel electrophoresis of the comet assay can use to evaluate the DNA damage after treatment with MB-SiO₂@MSNs-IMD-Cu and MB-SiO₂@MSNs-Cu-Dox nanoparticles (50 μ g/mL). The treated cells (1×10^5 /mL, 5 μ L) were mixed with 50 μ L of Comet low-melting agarose and then added to 50 μ L of the above mixtures and placed onto CometSlide™. Slides were immersed in 4 °C lysis solution (60 min), drained excess buffer, and then immersed in alkaline unwinding solution (4 °C for 1 h). Further, slides were placed in the alkaline electrophoresis solution to perform at 21 V, 300 mA for 20 min. DNA was stained by adding 100 μ L of Sybr green (1:10,000 dilution) for 30 min. The DNA damage was measured by fluorescent microscope (Ex/Em: 496/522 nm).

3.12. DCFH-DA Assay

Briefly, a DCFH-DA fluorescent probe was applied to detect the production of intracellular ROS levels. The cells were cultured in a 6-well plate at a density of 2×10^5 cells/well for 24 h. After appropriate cell attachment, various nanoparticles (50 μ g/mL) were added to the culture medium and incubated for 4 h. Cells were further washed with PBS twice and 10 μ M DCFH-DA was added in each well and incubated for 30 min. The cells were then washed with PBS, and PDT groups were further exposed to the LED 630 nm (15 mW/cm²) for 15 min and then incubated for 12 h. Finally, the cells were analyzed by flow cytometry to determine the fluorescent intensity.

3.13. ESR Spin Trapping

To explore the free radical production of MB-SiO₂@MSNs-Cu and MB-SiO₂@MSNs-Cu-Dox samples through the cupric catalysis of Fenton-like reaction with H₂O₂, the ESR spin-trapping technique was studied by using DMPO as a free radical trapping agent. The experimental conditions for a typical reaction included 6 mg of nanoparticles, 50 μ L of 100 mM DMPO, 50 μ L of 50 mM H₂O₂, and H₂O (400 μ L). After vigorous vortexing of

the mixture for 20 s, the solids were removed by syringe filters. The ESR spectra of the extracted liquid were recorded after mixing for 3 min.

4. Conclusions

The MB-SiO₂ embedded mesoporous silica core-shell architectures were designed by initially incorporating MB in silica frameworks and further depositing mesoporous silica shells. Further, the surfactant template was successfully extracted and modified with imidazole silane to achieve Cu ion chelation and high loading of Dox in the nanochannels of MSNs. This material possesses large advantages in cancer studies, good controllable size and surface charge, and carries more than one drug at a time to inhibit tumor growth synergistically. These designed architectures were systematically characterized using various physicochemical characterization techniques and demonstrated the potent anti-cancer efficacy against skin melanoma. Together, our results demonstrated that the mesoporous silica-based core-shell nanoarchitectures shows great potential as an effective strategy in synergistically ablating cancer through chemo-, chemodynamic, and photodynamic therapies.

Author Contributions: Conceptualization, C.-H.L.; methodology, Y.-M.G. and S.-H.C.; software, Y.-M.G. and P.B.; validation, R.K.K. and C.-H.L.; formal analysis, Y.-M.G. and S.-H.C.; investigation, Y.-M.G., S.-H.C. and P.B.; resources, C.-L.L., C.-H.L.; data curation, R.K.K. and C.-H.L.; writing—original draft preparation, Y.-M.G., P.B., R.K.K. and C.-H.L.; writing—review and editing, R.K.K. and C.-H.L.; visualization, Y.-M.G., S.-H.C. and P.B.; supervision, R.K.K. and C.-H.L.; project administration, C.-H.L.; funding acquisition, C.-H.L. All authors have read and agreed to the published version of the manuscript.

Funding: This research was funded by the Ministry of Science and Technology, Taiwan, for financial support Grant Nos. MOST 110-2113-M-259-004 and 111-2113-M-259-003.

Institutional Review Board Statement: Not applicable.

Informed Consent Statement: Not applicable.

Data Availability Statement: Not applicable.

Conflicts of Interest: The authors declare no conflict of interest.

References

1. Miller, K.D.; Siegel, R.L.; Lin, C.C.; Mariotto, A.B.; Kramer, J.L.; Rowland, J.H.; Stein, K.D.; Alteri, R.; Jemal, A. Cancer treatment and survivorship statistics, 2016. *CA Cancer J. Clin.* **2016**, *66*, 271–289. [[CrossRef](#)]
2. Dizon, D.S.; Krilov, L.; Cohen, E.; Gangadhar, T.; Ganz, P.A.; Hensing, T.A.; Hunger, S.; Krishnamurthi, S.S.; Lassman, A.B.; Markham, M.; et al. Clinical Cancer Advances 2016: Annual Report on Progress Against Cancer From the American Society of Clinical Oncology. *J. Clin. Oncol.* **2016**, *34*, 987–1011. [[CrossRef](#)]
3. Bhargava, R.; Sahoo, S.; Esposito, N.N.; Chen, B. Pathology of Breast Carcinoma: Diagnostic, Prognostic, and Therapeutic Issues and Challenges. *Pathol. Res. Int.* **2011**, *2011*, 731470–731472. [[CrossRef](#)]
4. Harris, T.J.R.; McCormick, F. The molecular pathology of cancer. *Nat. Rev. Clin. Oncol.* **2010**, *7*, 251–265. [[CrossRef](#)]
5. Arruebo, M.; Vilaboa, N.; Sáez-Gutierrez, B.; Lambea, J.; Tres, A.; Valladares, M.; González-Fernández, Á. Assessment of the Evolution of Cancer Treatment Therapies. *Cancers* **2011**, *3*, 3279–3330. [[CrossRef](#)]
6. Sudhakar, A. History of Cancer, Ancient and Modern Treatment Methods. *J. Cancer Sci. Ther.* **2009**, *1*, 1–4. [[CrossRef](#)]
7. Das, R.K.; Pramanik, A.; Majhi, M.; Mohapatra, S. Magnetic Mesoporous Silica Gated with Doped Carbon Dot for Site-Specific Drug Delivery, Fluorescence, and MR Imaging. *Langmuir* **2018**, *34*, 5253–5262. [[CrossRef](#)]
8. Mamaeva, V.; Rosenholm, J.M.; Bate-Eya, L.T.; Bergman, L.; Peuhu, E.; Duchanoy, A.; Fortelius, L.E.; Landor, S.; Toivola, D.M.; Lindén, M.; et al. Mesoporous Silica Nanoparticles as Drug Delivery Systems for Targeted Inhibition of Notch Signaling in Cancer. *Mol. Ther.* **2011**, *19*, 1538–1546. [[CrossRef](#)]
9. Duo, Y.; Li, Y.; Chen, C.; Liu, B.; Wang, X.; Zeng, X.; Chen, H. DOX-loaded pH-sensitive mesoporous silica nanoparticles coated with PDA and PEG induce pro-death autophagy in breast cancer. *RSC Adv.* **2017**, *7*, 39641–39650. [[CrossRef](#)]
10. Saroj, S.; Rajput, S.J. Tailor-made pH-sensitive polyacrylic acid functionalized mesoporous silica nanoparticles for efficient and controlled delivery of anti-cancer drug Etoposide. *Drug Dev. Ind. Pharm.* **2018**, *44*, 1198–1211. [[CrossRef](#)]
11. Lehman, S.E.; Morris, A.S.; Mueller, P.S.; Salem, A.; Grassian, V.H.; Larsen, S.C. Silica nanoparticle-generated ROS as a predictor of cellular toxicity: Mechanistic insights and safety by design. *Environ. Sci. Nano* **2016**, *3*, 56–66. [[CrossRef](#)]

12. Tao, W.; He, Z. ROS-responsive drug delivery systems for biomedical applications. *Asian J. Pharm. Sci.* **2018**, *13*, 101–112. [[CrossRef](#)]
13. Joshi, G.N.; Goetjen, A.M.; Knecht, D.A. Silica particles cause NADPH oxidase-independent ROS generation and transient phagolysosomal leakage. *Mol. Biol. Cell* **2015**, *26*, 3150–3164. [[CrossRef](#)]
14. Morry, J.; Ngamcherdtrakul, W.; Yantasee, W. Oxidative stress in cancer and fibrosis: Opportunity for therapeutic intervention with antioxidant compounds, enzymes, and nanoparticles. *Redox Biol.* **2017**, *11*, 240–253. [[CrossRef](#)]
15. Sui, B.; Zhong, G.; Sun, J. Drug-loadable Mesoporous Bioactive Glass Nanospheres: Biodistribution, Clearance, BRL Cellular Location and Systemic Risk Assessment via ⁴⁵Ca Labelling and Histological Analysis. *Sci. Rep.* **2016**, *6*, 33443. [[CrossRef](#)]
16. Weinberg, F.; Hamanaka, R.; Wheaton, W.W.; Weinberg, S.; Joseph, J.; Lopez, M.; Kalyanaraman, B.; Mutlu, G.M.; Budinger, G.R.S.; Chandel, N.S. Mitochondrial metabolism and ROS generation are essential for Kras-mediated tumorigenicity. *Proc. Natl. Acad. Sci. USA* **2010**, *107*, 8788. [[CrossRef](#)]
17. Tang, L.; Cheng, J. Nonporous silica nanoparticles for nanomedicine application. *Nano Today* **2013**, *8*, 290–312. [[CrossRef](#)]
18. Kim, K.S.; Lee, D.; Song, C.G.; Kang, P.M. Reactive oxygen species-activated nanomaterials as theranostic agents. *Nanomedicine* **2015**, *10*, 2709–2723. [[CrossRef](#)]
19. Fu, P.P.; Xia, Q.; Hwang, H.-M.; Ray, P.C.; Yu, H. Mechanisms of nanotoxicity: Generation of reactive oxygen species. *J. Food Drug Anal.* **2014**, *22*, 64–75. [[CrossRef](#)]
20. Yang, L.; Zhu, X.; Wang, H.; Zheng, L.; Zhong, Z.; Li, X.; Zhao, J.; Kou, J.; Jiang, Y.; Zheng, X.; et al. Upconversion nanoparticle-mediated photodynamic therapy induces THP-1 macrophage apoptosis via ROS bursts and activation of the mitochondrial caspase pathway. *Int. J. Nanomed.* **2015**, *10*, 3719–3736. [[CrossRef](#)]
21. Rao, V.N.; Han, H.S.; Lee, H.; Nguyen, V.Q.; Jeon, S.; Jung, D.-W.; Lee, J.; Yi, G.-R.; Park, J.H. ROS-responsive mesoporous silica nanoparticles for MR imaging-guided photodynamically maneuvered chemotherapy. *Nanoscale* **2018**, *10*, 9616–9627. [[CrossRef](#)]
22. Hong, E.J.; Choi, D.G.; Shim, M.S. Targeted and effective photodynamic therapy for cancer using functionalized nanomaterials. *Acta Pharm. Sin. B* **2016**, *6*, 297–307. [[CrossRef](#)]
23. Chou, C.-C.; Chen, W.; Hung, Y.; Mou, C.-Y. Molecular Elucidation of Biological Response to Mesoporous Silica Nanoparticles in Vitro and in Vivo. *ACS Appl. Mater. Interfaces* **2017**, *9*, 22235–22251. [[CrossRef](#)]
24. Tai, G.; Liu, G.; Li, Q.; Ni, W.; Zhang, N.; Zheng, X.; Wang, Y.; Shao, D. Cytotoxicity of various types of gold-mesoporous silica nanoparticles in human breast cancer cells. *Int. J. Nanomed.* **2015**, *10*, 6075–6087. [[CrossRef](#)]
25. Elle, R.E.; Rahmani, S.; Lauret, C.; Morena, M.; Bidet, L.P.R.; Boulahtouf, A.; Balaguer, P.; Cristol, J.-P.; Durand, J.-O.; Charnay, C.; et al. Functionalized Mesoporous Silica Nanoparticle with Antioxidants as a New Carrier That Generates Lower Oxidative Stress Impact on Cells. *Mol. Pharm.* **2016**, *13*, 2647–2660. [[CrossRef](#)]
26. Krętowski, R.; Kusaczuk, M.; Naumowicz, M.; Kotyńska, J.; Szyńska, B.; Cechowska-Pasko, M. The Effects of Silica Nanoparticles on Apoptosis and Autophagy of Glioblastoma Cell Lines. *Nanomaterials* **2017**, *7*, 230. [[CrossRef](#)]
27. Tang, X.-l.; Jing, F.; Lin, B.-l.; Cui, S.; Yu, R.-t.; Shen, X.-d.; Wang, T.-w. pH-Responsive Magnetic Mesoporous Silica-Based NanoplatforM for Synergistic Photodynamic Therapy/Chemotherapy. *ACS Appl. Mater. Interfaces* **2018**, *10*, 15001–15011. [[CrossRef](#)]
28. Zhang, W.; Shen, J.; Su, H.; Mu, G.; Sun, J.-H.; Tan, C.-P.; Liang, X.-J.; Ji, L.-N.; Mao, Z.-W. Co-Delivery of Cisplatin Prodrug and Chlorin e6 by Mesoporous Silica Nanoparticles for Chemo-Photodynamic Combination Therapy to Combat Drug Resistance. *ACS Appl. Mater. Interfaces* **2016**, *8*, 13332–13340. [[CrossRef](#)]
29. Yan, T.; Cheng, J.; Liu, Z.; Cheng, F.; Wei, X.; He, J. pH-Sensitive mesoporous silica nanoparticles for chemo-photodynamic combination therapy. *Colloids Surf. B Biointerfaces* **2018**, *161*, 442–448. [[CrossRef](#)]
30. Li, H.; Wei, M.; Lv, X.; Hu, Y.; Shao, J.; Song, X.; Yang, D.; Wang, W.; Li, B.; Dong, X. Cerium-based Nanoparticles for Cancer Photodynamic Therapy. *J. Innov. Opt. HealthSci.* **2022**. [[CrossRef](#)]
31. Zhang, Y.; Du, H.; He, P.; Shen, C.; Li, Q.; Duan, Y.; Shao, Z.; Mu, F.; Huang, F.; Li, P.; et al. Exfoliated FePS₃ nanosheets for T1-weighted magnetic resonance imaging-guided near-infrared photothermal therapy in vivo. *Sci. China Mater.* **2021**, *64*, 2613–2623. [[CrossRef](#)]
32. Wang, K.; Zhang, Y.; Wang, J.; Yuan, A.; Sun, M.; Wu, J.; Hu, Y. Self-assembled IR780-loaded transferrin nanoparticles as an imaging, targeting and PDT/PTT agent for cancer therapy. *Sci. Rep.* **2016**, *6*, 27421. [[CrossRef](#)]
33. Hovan, A.; Datta, S.; Kruglik, S.G.; Jancura, D.; Miskovsky, P.; Bánó, G. Phosphorescence Kinetics of Singlet Oxygen Produced by Photosensitization in Spherical Nanoparticles. Part I. Theory. *J. Phys. Chem. B* **2018**, *122*, 5147–5153. [[CrossRef](#)]
34. Kankala, R.K.; Han, Y.-H.; Na, J.; Lee, C.-H.; Sun, Z.; Wang, S.-B.; Kimura, T.; Ok, Y.S.; Yamauchi, Y.; Chen, A.-Z.; et al. Nanoarchitected Structure and Surface Biofunctionality of Mesoporous Silica Nanoparticles. *Adv. Mater.* **2020**, *32*, 1907035. [[CrossRef](#)]
35. Kankala, R.K.; Han, Y.-H.; Xia, H.-Y.; Wang, S.-B.; Chen, A.-Z. Nanoarchitected prototypes of mesoporous silica nanoparticles for innovative biomedical applications. *J. Nanobiotechnol.* **2022**, *20*, 126. [[CrossRef](#)]
36. Kankala, R.K.; Wang, S.-B.; Chen, A.-Z. Nanoarchitecting Hierarchical Mesoporous Siliceous Frameworks: A New Way Forward. *iScience* **2020**, *23*, 101687. [[CrossRef](#)]
37. Gartmann, N.; Brühwiler, D. Controlling and Imaging the Functional-Group Distribution on Mesoporous Silica. *Angewandte Chem. Int. Ed.* **2009**, *48*, 6354–6356. [[CrossRef](#)]

38. Freitas, L.B.d.O.; Corgosinho, L.d.M.; Faria, J.A.Q.A.; dos Santos, V.M.; Resende, J.M.; Leal, A.S.; Gomes, D.A.; Sousa, E.M.B.d. Multifunctional mesoporous silica nanoparticles for cancer-targeted, controlled drug delivery and imaging. *Microporous Mesoporous Mater.* **2017**, *242*, 271–283. [[CrossRef](#)]
39. Bharti, C.; Nagaich, U.; Pal, A.K.; Gulati, N. Mesoporous silica nanoparticles in target drug delivery system: A review. *Int. J. Pharm. Investig.* **2015**, *5*, 124–133. [[CrossRef](#)]
40. Shi, S.; Chen, F.; Cai, W. Biomedical Applications of Functionalized Hollow Mesoporous Silica Nanoparticles: Focusing on Molecular Imaging. *Nanomedicine* **2013**, *8*, 10–2217. [[CrossRef](#)]
41. Dai, L.; Zhang, Q.; Li, J.; Shen, X.; Mu, C.; Cai, K. Dendrimerlike Mesoporous Silica Nanoparticles as pH-Responsive Nanocontainers for Targeted Drug Delivery and Bioimaging. *ACS Appl. Mater. Interfaces* **2015**, *7*, 7357–7372. [[CrossRef](#)] [[PubMed](#)]
42. Maggini, L.; Cabrera, I.; Ruiz-Carretero, A.; Prasetyanto, E.A.; Robinet, E.; De Cola, L. Breakable mesoporous silica nanoparticles for targeted drug delivery. *Nanoscale* **2016**, *8*, 7240–7247. [[CrossRef](#)] [[PubMed](#)]
43. Kim, M.-H.; Na, H.-K.; Kim, Y.-K.; Ryoo, S.-R.; Cho, H.S.; Lee, K.E.; Jeon, H.; Ryoo, R.; Min, D.-H. Facile Synthesis of Monodispersed Mesoporous Silica Nanoparticles with Ultralarge Pores and Their Application in Gene Delivery. *ACS Nano* **2011**, *5*, 3568–3576. [[CrossRef](#)] [[PubMed](#)]
44. Chang, F.-P.; Kuang, L.-Y.; Huang, C.-A.; Jane, W.-N.; Hung, Y.; Hsing, Y.-i.C.; Mou, C.-Y. A simple plant gene delivery system using mesoporous silica nanoparticles as carriers. *J. Mater. Chem. B* **2013**, *1*, 5279–5287. [[CrossRef](#)] [[PubMed](#)]
45. Kankala, R.K.; Zhang, H.; Liu, C.-G.; Kanubaddi, K.R.; Lee, C.-H.; Wang, S.-B.; Cui, W.; Santos, H.A.; Lin, K.; Chen, A.-Z. Metal Species-Encapsulated Mesoporous Silica Nanoparticles: Current Advancements and Latest Breakthroughs. *Adv. Funct. Mater.* **2019**, *29*, 1902652. [[CrossRef](#)]
46. Planas, O.; Bresolí-Obach, R.; Nos, J.; Gallavardin, T.; Ruiz-González, R.; Agut, M.; Nonell, S. Synthesis, Photophysical Characterization, and Photoinduced Antibacterial Activity of Methylene Blue-loaded Amino- and Mannose-Targeted Mesoporous Silica Nanoparticles. *Molecules* **2015**, *20*, 6284–6298. [[CrossRef](#)]
47. Lv, J.; Wu, G.; He, Y.; Zhang, L.; Yi, Y. Methylene blue-loaded gold nanobipyramids @SiO₂ enhanced singlet oxygen generation for phototherapy of cancer cells. *Opt. Mater. Express* **2017**, *7*, 409–414. [[CrossRef](#)]
48. Hanafi-Bojd, M.Y.; Jaafari, M.R.; Ramezani, N.; Xue, M.; Amin, M.; Shahtahmassebi, N.; Malaekhe-Nikouei, B. Surface functionalized mesoporous silica nanoparticles as an effective carrier for epirubicin delivery to cancer cells. *Eur. J. Pharm. Biopharm.* **2015**, *89*, 248–258. [[CrossRef](#)]
49. Wani, A.; Muthuswamy, E.; Savithra, G.H.L.; Mao, G.; Brock, S.; Oupický, D. Surface Functionalization of Mesoporous Silica Nanoparticles Controls Loading and Release Behavior of Mitoxantrone. *Pharm. Res.* **2012**, *29*, 2407–2418. [[CrossRef](#)]
50. Smith, M.A.; Iiasi, M.G.; Zoelle, A. A Novel Approach to Calibrate Mesopore Size from Nitrogen Adsorption Using X-ray Diffraction: An SBA-15 Case Study. *J. Phys. Chem. C* **2013**, *117*, 17493–17502. [[CrossRef](#)]
51. Huang, I.P.; Sun, S.-P.; Cheng, S.-H.; Lee, C.-H.; Wu, C.-Y.; Yang, C.-S.; Lo, L.-W.; Lai, Y.-K. Enhanced Chemotherapy of Cancer Using pH-Sensitive Mesoporous Silica Nanoparticles to Antagonize P-Glycoprotein-Mediated Drug Resistance. *Mol. Cancer Ther.* **2011**, *10*, 761–769. [[CrossRef](#)] [[PubMed](#)]
52. Manzanares, D.; Ceña, V. Endocytosis: The Nanoparticle and Submicron Nanocompounds Gateway into the Cell. *Pharmaceutics* **2020**, *12*, 371. [[CrossRef](#)] [[PubMed](#)]
53. Oh, N.; Park, J.H. Endocytosis and exocytosis of nanoparticles in mammalian cells. *Int. J. Nanomed.* **2014**, *9* (Suppl. S1), 51–63. [[CrossRef](#)]
54. Belhekar, A.A.; Awate, S.V.; Anand, R. Photocatalytic activity of titania modified mesoporous silica for pollution control. *Catal. Commun.* **2002**, *3*, 453–458. [[CrossRef](#)]
55. Haque, E.; Jun, J.W.; Jhung, S.H. Adsorptive removal of methyl orange and methylene blue from aqueous solution with a metal-organic framework material, iron terephthalate (MOF-235). *J. Hazard. Mater.* **2011**, *185*, 507–511. [[CrossRef](#)]
56. Shibu, E.S.; Hamada, M.; Murase, N.; Biju, V. Nanomaterials formulations for photothermal and photodynamic therapy of cancer. *J. Photochem. Photobiol. C Photochem. Rev.* **2013**, *15*, 53–72. [[CrossRef](#)]
57. Ahmed, N.; Fessi, H.; Elaissari, A. Theranostic applications of nanoparticles in cancer. *Drug Discov. Today* **2012**, *17*, 928–934. [[CrossRef](#)]
58. Wang, T.; Zhang, L.; Su, Z.; Wang, C.; Liao, Y.; Fu, Q. Multifunctional Hollow Mesoporous Silica Nanocages for Cancer Cell Detection and the Combined Chemotherapy and Photodynamic Therapy. *ACS Appl. Mater. Interfaces* **2011**, *3*, 2479–2486. [[CrossRef](#)]
59. Makhadmeh, G.N.; Abdul Aziz, A.; Abdul Razak, K. The efficacy of methylene blue encapsulated in silica nanoparticles compared to naked methylene blue for photodynamic applications. *Artif. Cells Nanomed. Biotechnol.* **2016**, *44*, 1018–1022. [[CrossRef](#)]
60. Kohle, F.F.E.; Li, S.; Turker, M.Z.; Wiesner, U.B. Ultrasmall PEGylated and Targeted Core-Shell Silica Nanoparticles Carrying Methylene Blue Photosensitizer. *ACS Biomater. Sci. Eng.* **2020**, *6*, 256–264. [[CrossRef](#)]
61. Malinge, J.; Allain, C.; Galmiche, L.; Miomandre, F.; Audebert, P. Preparation, Photophysical, Electrochemical, and Sensing Properties of Luminescent Tetrazine-Doped Silica Nanoparticles. *Chem. Mater.* **2011**, *23*, 4599–4605. [[CrossRef](#)]
62. Cheng, S.-H.; Lee, C.-H.; Yang, C.-S.; Tseng, F.-G.; Mou, C.-Y.; Lo, L.-W. Mesoporous silica nanoparticles functionalized with an oxygen-sensing probe for cell photodynamic therapy: Potential cancer theranostics. *J. Mater. Chem.* **2009**, *19*, 1252–1257. [[CrossRef](#)]

63. Li, Z.; Barnes, J.C.; Bosoy, A.; Stoddart, J.F.; Zink, J.I. Mesoporous silica nanoparticles in biomedical applications. *Chem. Soc. Rev.* **2012**, *41*, 2590–2605. [[CrossRef](#)]
64. Yang, P.; Gai, S.; Lin, J. Functionalized mesoporous silica materials for controlled drug delivery. *Chem. Soc. Rev.* **2012**, *41*, 3679–3698. [[CrossRef](#)] [[PubMed](#)]
65. Kang, T.; Park, Y.; Choi, K.; Lee, J.S.; Yi, J. Ordered mesoporous silica (SBA-15) derivatized with imidazole-containing functionalities as a selective adsorbent of precious metal ions. *J. Mater. Chem.* **2004**, *14*, 1043–1049. [[CrossRef](#)]
66. Lee, C.-H.; Lin, T.-S.; Mou, C.-Y. (VO)₂⁺ Ions Immobilized on Functionalized Surface of Mesoporous Silica and Their Activity toward the Hydroxylation of Benzene. *J. Phys. Chem. B* **2003**, *107*, 2543–2551. [[CrossRef](#)]
67. Kankala, R.K.; Tsai, P.-Y.; Kuthati, Y.; Wei, P.-R.; Liu, C.-L.; Lee, C.-H. Overcoming multidrug resistance through co-delivery of ROS-generating nano-machinery in cancer therapeutics. *J. Mater. Chem. B* **2017**, *5*, 1507–1517. [[CrossRef](#)]
68. Shen, J.; He, Q.; Gao, Y.; Shi, J.; Li, Y. Mesoporous silica nanoparticles loading doxorubicin reverse multidrug resistance: Performance and mechanism. *Nanoscale* **2011**, *3*, 4314–4322. [[CrossRef](#)]
69. Kankala, R.K.; Liu, C.-G.; Chen, A.-Z.; Wang, S.-B.; Xu, P.-Y.; Mende, L.K.; Liu, C.-L.; Lee, C.-H.; Hu, Y.-F. Overcoming multidrug resistance through the synergistic effects of hierarchical pH-sensitive, ROS-generating nanoreactors. *ACS Biomater. Sci. Eng.* **2017**, *3*, 2431–2442. [[CrossRef](#)]
70. Shahabi, S.; Döscher, S.; Bollhorst, T.; Treccani, L.; Maas, M.; Dringen, R.; Rezwani, K. Enhancing Cellular Uptake and Doxorubicin Delivery of Mesoporous Silica Nanoparticles via Surface Functionalization: Effects of Serum. *ACS Appl. Mater. Interfaces* **2015**, *7*, 26880–26891. [[CrossRef](#)]
71. Slowing, I.; Trewyn, B.G.; Lin, V.S.Y. Effect of Surface Functionalization of MCM-41-Type Mesoporous Silica Nanoparticles on the Endocytosis by Human Cancer Cells. *J. Am. Chem. Soc.* **2006**, *128*, 14792–14793. [[CrossRef](#)] [[PubMed](#)]